Rational design of Lewis base molecules for stable and efficient inverted perovskite solar cells

Authors: Chongwen Li[1], Xiaoming Wang[1], Enbing Bi[1], Fangyuan Jiang[2], So Min Park[3], You Li[1], Lei Chen[1], Zaiwei Wang[3], Lewei Zeng[3], Hao Chen[3], Yanjiang Liu[3], Corey R. Grice[1,4], Abasi Abudulimu[1], Jaehoon Chung[1], Yeming Xian[1], Tao Zhu[1], Huagui Lai[5], Bin Chen[3,6], Randy J. Ellingson[1], Fan Fu[5], David S. Ginger[2], Zhaoning Song[1], Edward H. Sargent[3,6,7], Yanfa Yan[1*]

Affiliations:

[1]Department of Physics and Astronomy and Wright Center for Photovoltaics Innovation and Commercialization, The University of Toledo, Toledo, Ohio 43606, United States.

[2]Department of Chemistry, University of Washington, Seattle, Washington 98195, United States

[3]The Edward S. Rogers Department of Electrical and Computer Engineering, University of Toronto, Toronto, Ontario M5S 3G4, Canada

[4]Center for Materials and Sensors Characterization, The University of Toledo, Toledo, Ohio 43606, United States.

[5]Laboratory for Thin Films and Photovoltaics, Empa–Swiss Federal Laboratories for Materials Science and Technology, Duebendorf 8600, Switzerland.

[6]Department of Chemistry, Northwestern University, Evanston, Illinois 60208, United States.

[7]Department of Electrical and Computer Engineering, Northwestern University, Evanston, Illinois 60208, United States.

*Corresponding author. Email: yanfa.yan@utoledo.edu

Abstract: Lewis-base molecules that bind undercoordinated Pb atoms at interfaces and grain boundaries (GBs) are known to enhance the durability of metal halide perovskite solar cells (PSCs). Using density functional theory calculations, we found that phosphine (P)-containing molecules have the strongest binding energy among members of a library of Lewis base molecules studied herein. Experimentally, we found that the best inverted PSC treated using 1,3-bis(diphenylphosphino)propane (DPPP), a diphosphine Lewis base which passivates, binds, and bridges interfaces and GBs, retained a power conversion efficiency (PCE) slightly higher than its initial PCE of ~23% following continuous operation under simulated AM1.5 illumination at the maximum power point and at ~40°C for >3,500 hours. DPPP-treated devices showed a similar increase in PCE after being kept at open-circuit and at 85 Celsius for >1,500 hours.

One-Sentence Summary: The Lewis base molecule DPPP enables inverted perovskite solar cells with superior stability under both operating and open circuit accelerated ageing conditions.

Main Text:

Metal halide perovskite solar cells (PSCs) offer a route to lowering the cost of solar electricity given their high power conversion efficiencies (PCEs) (*1-4*). However, durability remains a major hurdle along the path to technological relevance (*5-7*) and must be assessed through accelerated degradation tests (*8*). Damp-heat testing at 85°C in dark and 85% relative humidity (RH), a test standard for crystalline silicon (Si) and thin-film PV modules, has been adopted for accelerating the durability test of PSCs (*9 - 11*). These tests are typically used to evaluate packaging rather than PV material durability. PSCs can also show degradation under photoexcited conditions (*12*), and especially at open-circuit (OC) conditions (*13*), that are more acute than one sees in standardized silicon tests. Mechanistically, such this findings are often assigned to ion migration (*14, 15*) and charge accumulation at interfaces (*9, 16,17*).

We studied the operating stability at 85°C under simulated one sun illumination and OC conditions – important test conditions under which PSCs have been studied to date only to a limited degree (*18-20*). Light- and heat-induced degradation in PSCs is related to point defects formed at interfaces and grain boundaries (GBs) (*14, 21*). Moisture-induced degradation is curtailed using encapsulation (*22*); whereas the passivation of defects at interfaces and GBs within the perovskite film is required to improve the PCE and intrinsic durability of PSCs (*11, 23-26*). Particular promise in increasing durability has been seen in the use of P-, N-, S-, and O-containing Lewis-base molecules to form coordinate covalent bonds (dative bonds) that donate electrons to undercoordinated Pb atoms at interfaces and GBs (*27-29*).

Using density functional theory (DFT), we saw evidence that P-containing Lewis base molecules showed the strongest binding with uncoordinated Pb atoms. We thus pursued diphosphine-containing molecules, reasoning that these would provide additional binding and bridging at interfaces and GBs. For experimental studies we selected 1,3-bis(diphenylphosphino)propane (DPPP), a diphosphine Lewis base. We found that treating perovskites with a small amount of DPPP improves PCE and durability: inverted (*p-i-n*) PSCs after DPPP treatment showed a champion PCE of 24.5%. A DPPP-treated PSC with an initial PCE of ~23% stabilized at ~23.5% after maximum power point (MPP) tracking under continuous simulated AM1.5 illumination at ~40°C for >3,500 hours. DPPP-stabilized PSCs showed no PCE degradation after being kept at OC and 85°C conditions for >1,500 hours.

Bonding interactions of Lewis bases

The P, N, S, and O atoms in Lewis base molecules donate electrons to the Lewis acid sites in perovskites, such as the undercoordinated Pb^{2+} at perovskite surfaces, in order to form coordinate covalent bonds. In general, the Lewis basicity, which is inversely proportional to electronegativity, is expected to determine the binding energy and the stabilization of interfaces and GBs. We compared binding energies of prototypical Lewis bases, trimethylphosphine (TMP), trimethylamine (TMA), dimethylsulfide (DMS), and dimethylether (DME), with sp^3 hybridization to the surface of $FAPbI_3$ through DFT calculations (Fig. 1A). The calculated binding strength followed the order P > N > S > O, indicating the electronegativity rule did not strictly apply – a finding we attribute to the remaining lone pair electrons in the case of S and O following binding with perovskites. We also compared frequently-reported Lewis base molecules with the sp^2 oxygen in the carbonyl groups and took acetone and methyl acetate (MeOAc) as examples in Fig. 1A (*26, 30*). The binding energies were similar to that of DME.

Lewis base molecules have mostly been used to passivate uncoordinated Pb atoms (*24, 31 - 33*). A Lewis base molecule with two electron donating atoms can potentially bind and bridge interfaces and GBs, offering the potential to enhance the adhesion and strengthen the mechanical toughness of PSCs and provide additional benefits related to the durability of PSCs. For this reason, we selected DPPP, a diphosphine Lewis base molecule in seeking to stabilize and passivate PSCs. As shown in Fig. 1B and fig. S1, a DPPP molecule has two P atoms with sp^3 hybridization in tetrahedral coordination. The lone pair electrons occupy the missing vertex of the tetrahedron, and if donated to Lewis acids (metal cations) to form a covalent bond, the fully tetrahedral coordination would realize and gain more stabilization.

We calculated the binding of DPPP on the surfaces of $FAPbI_3$ both with PbI_2 and FAI terminations. Although DFT calculations predicted that the FAI terminated surface was more stable (*34*), experimental evidence showed that the PbI_2 terminated surface is readily formed during the solvent treatment from depositing subsequent layers (*35*). DFT calculations also showed that DPPP was chemically bonded to the PbI_2 terminated surface through P-Pb bond formation with a binding energy of 2.24 eV but was weakly bonded to the FAI-terminated surface by the van der Waals interaction with a binding energy of 1.09 eV (Fig. 1, C and D).

Moreover, the calculated binding energy of DPPP with perovskites in two adjacent slabs (3.08 eV) was larger than that in the same slab (2.24 eV) (Fig. 1, D and E). Similarly, the binding energy of DPPP with both the perovskite and NiO_x slabs (4.31 eV) was larger than that (3.28 eV) in the same NiO_x slab (Fig. 1F and fig. S2). Thus, DPPP was predicted to bind, bridge and stabilize perovskite GBs and perovskite/NiO_x interface. DPPP molecules also provided hole transport channels through the P-terminated alkane chain of DPPP (fig. S3).

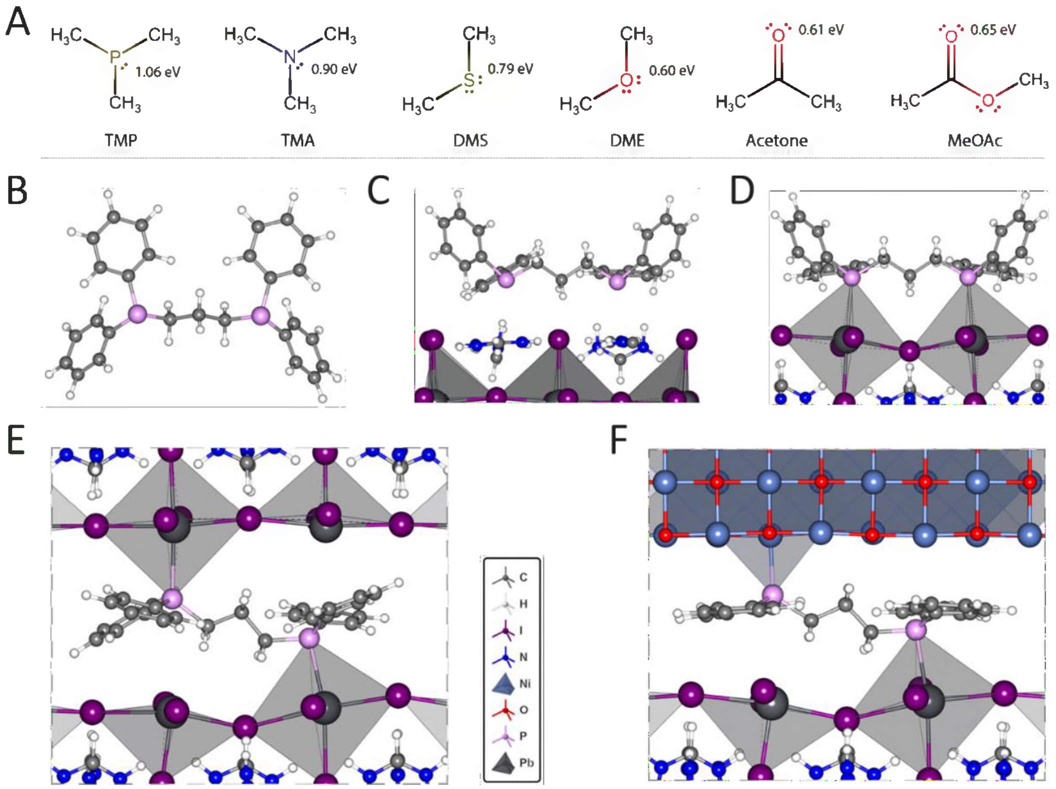

Fig. 1. DFT calculated DPPP binding with perovskites. (**A**) Chemical structures of prototypical Lewis base molecules. The numbers are the DFT-calculated binding energies (in eV) of the Lewis base molecule bonded to the $FAPbI_3$ surface with PbI_2 termination. (**B**) Molecular structure of DPPP. The P atom of DPPP donates a lone-pair electron to the metal cation forming a coordinate covalent bond. Covalent bonding and van der Waals bonding for DPPP bound on $FAPbI_3$ surfaces with (**C**) FAI and (**D**) PbI_2 terminations, respectively. DPPP binds (**E**) two perovskite slabs and (**F**) perovskite and NiO_x substrate through chemical-bond formation between P and Pb/Ni atoms in a Lewis acid-base reaction.

Synthesis and structure

The interaction between DPPP molecules and Pb^{2+} is seen via the formation of a new adduct when a thin layer of DPPP was deposited on a PbI_2 layer (fig. S4). When fabricating devices, we deposited the FA-based perovskite layer on DPPP coated NiO_x hole transport layer. During the growth of perovskite films, some DPPP molecules re-dissolved and segregated at both the perovskite/NiO_x interface and the perovskite surface regions, as verified by the time-of-flight secondary ion mass spectrometry (ToF-SIMS) depth profiles shown in Fig. 2A. X-ray photoelectron spectroscopy (XPS) revealed that after DPPP treatment, the core levels of the elements in both perovskite and NiO_x shifted (Pb and Ni XPS spectra in Fig. 2B and Fig 2C and the O, C, N, and I spectra in fig. S5). The universal shift of core levels caused by electrostatic interaction indicates the existence of DPPP at both the interfaces. The DPPP treatment also slightly improved the crystallinity of perovskite films, as can be seen from the enhancement of grain domain size (fig. S6) and XRD peak intensity (fig. S7). DPPP treatment did not change the bandgap of the perovskite films (fig. S8). Photoluminescence (PL) and time-resolved PL spectroscopy (TRPL) spectra (Fig. 2, D and E) showed enhanced PL intensity and ~50% improved lifetime from 0.98 to 1.49 μs for the DPPP-treated perovskite films, consistent with the expected reduction in nonradiative recombination and defect density upon Lewis-base treatment (*29*, *36*). We further verified that DPPP treatment enhanced the mechanical toughness of the perovskite/NiO_x interface. Perovskite films were deposited on a half-cell structure with and without DPPP treatment, protected by a thin PMMA layer, and adhered to a glass plate with epoxy (see details in the Supplementary Materials and fig. S9). A tensile load was applied to delaminate the films using a testing machine shown in fig. S10. After delamination, both the NiO_x and perovskite surfaces of the NiO_x/perovskite interface showed P signals, indicating DPPP remained on both surfaces (fig. S11). The tensile force recorded during the delamination process (Fig. 2F) suggest that DPPP treatment enhanced the mechanical strength of the perovskite/NiO_x interface through the binding of DPPP at the interface.

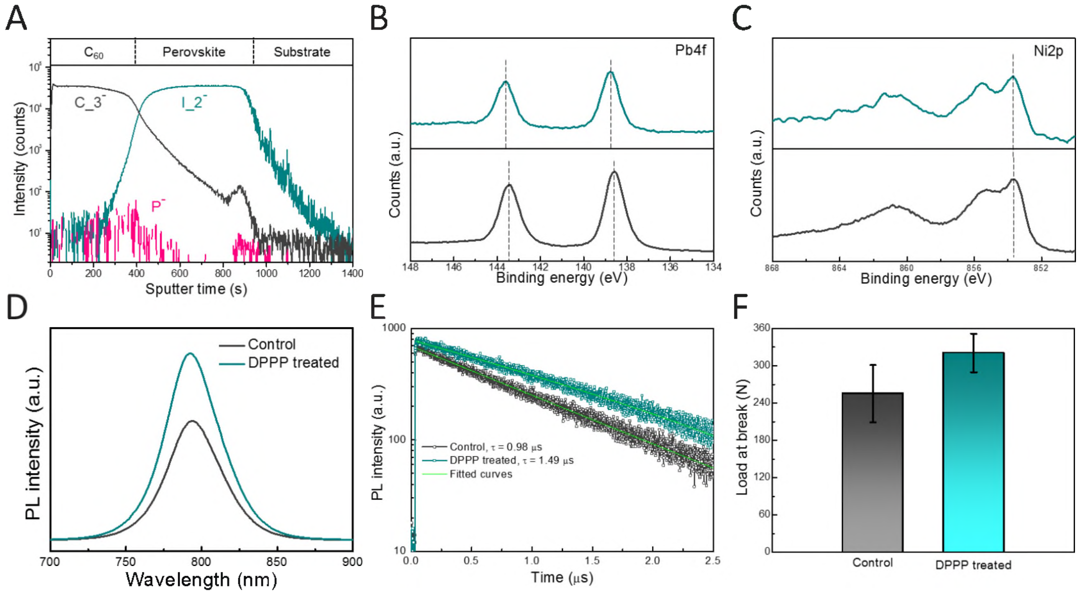

Fig. 2. Effects of DPPP on perovskite film quality and device performance. (**A**) ToF-SIMS depth profile of a DPPP-treated sample showing DPPP molecules segregate at both interfaces. XPS spectra comparing (**B**) binding energy of Pb-4f core levels of control and DPPP-treated samples and (**C**) binding energy of Ni-2p core levels of NiO_x before and after DPPP treatment. PL (D) and TRPL (E) spectra of control and DPPP-treated perovskite films measured from the film side. The samples were excited with a continuous-wave 633-nm laser at a fluence of 1.5×10^{17} photons $cm^{-2}s^{-1}$. (**F**) Histogram and standard deviation values of loads at break of 10 sets of control and DPPP-treated samples.

Hyperspectral PL mapping measured from the buried interfaces and PL intensity histograms in Fig. 3, A to D revealed an overall higher PL intensity of the DPPP-treated perovskite film that was consistent with the longer PL lifetimes and indicated reduced defect density as compared to the control perovskite films. The PL emission heterogeneity increased and more dark spots were observed over time in the control film after light aging (fig. S12). These dark spots showed lower PL emission intensity, and we attributed them to the initial sites of photodegradation at localized defects and local heterogeneities, which were more prevalent in the control sample without DPPP. PL decay takes place mostly in regions with low initial PL counts, while PL enhancement takes place in regions with high initial PL counts (fig. S13). This observation proves that local PL enhancement/decay in the control sample is associated with local defect heterogeneities. In comparison, the DPPP-treated films exhibited higher uniformity and better light stability, with most of the pixels showing photo-brightening with increased PL counts, rather than photo-decay with decreased PL counts as was observed for the control perovskite film (Fig. 3, B and D and fig. S12). Scanning electron microscopy (SEM) images measured from the bottom surface show needle-shaped PbI_2 crystals on the as-prepared control film, which is likely caused by the excess PbI_2 added to the precursor solution (fig. S14A). The as-prepared DPPP-treated film showed distinct layered structures (fig. S14B), which we speculated could possibly be the Lewis acid-base adduct of PbI_2 and DPPP. After aging, the PbI_2 crystals in the control film decomposed and produced pinholes on the grains (Fig. 3E). In contrast, the DPPP-treated films exhibited much-suppressed degradation (Fig. 3F), consistent with the optical microscopy above. Time-resolved mass spectroscopy was also conducted on control and DPPP-treated films under illumination to investigate the degradation process. The control sample showed the release of HI and I species (fig. S15), which are by-products of the photoinduced decomposition and trigger irreversible chemical chain reactions that accelerate the decomposition of perovskites (*37, 38*). In addition to the iodide species, another perovskite decomposition by-product, metallic Pb_0, was also observed on the control film after light soaking. The XPS spectrum of the control film after light-soaking showed two Pb_0 peaks at ~136 and ~141 eV (Fig. 3G), whereas no Pb_0 peaks were observed in DPPP-treated film. These results reveal that DPPP treatment could effectively suppress the photodecomposition at the NiO_x/perovskite interface, likely by reducing the density of reactive undercoordinated lead sites (halide vacancies) at the surface and interfaces.

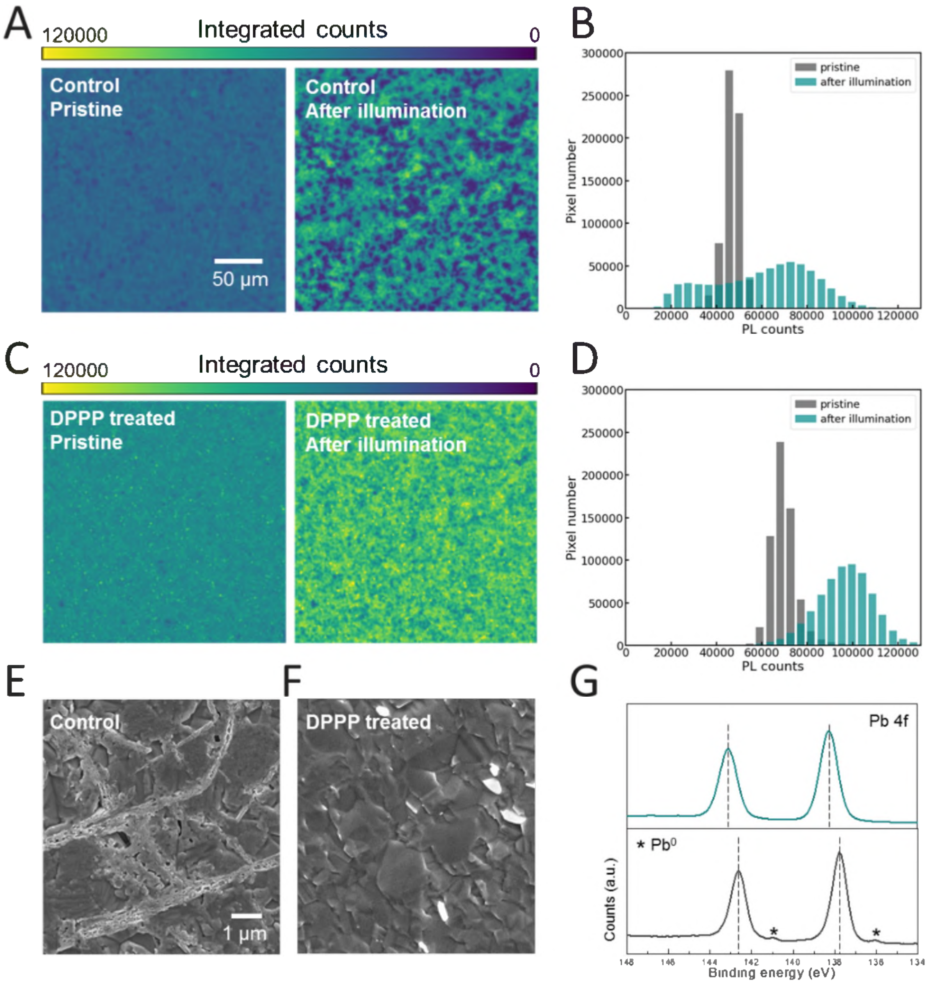

Fig. 3. Characterization of perovskite film stability before and after DPPP treatment. (A to **D**) Hyperspectral PL images and histograms of control and DPPP-treated perovskite films before and after light aging. The PL images were taken from the buried interface side, and the PL count at each pixel refers to the integrated PL counts over the whole spectrum. (**E** and **F**) SEM top-view images taken from the buried interface of control and DPPP-treated perovskite films after light soaking. (**G**) XPS measured from the buried interface of control and DPPP-treated perovskite films after light soaking.

Solar cell fabrication and performance

We fabricated PSCs with the *p-i-n* configuration of glass/FTO/NiO_x/Me-4PACz/(with or without) DPPP/$FA_{0.95}Cs_{0.05}PbI_3$/PEAI/C_{60}/SnO_2/Ag to show the effect of DPPP treatment on improving device performance and stability. Note that NiO_x was treated by a very thin layer of Me-4PACz to improve the reproducibility (fig. S16). The statistics of our device performance results are shown in fig. S17. A small amount of DPPP (1 or 2 mg/mL) consistently improved the open-circuit voltage (V_{OC}) and fill factor (FF) across the comparison of 40 devices. Both the improvement in V_{OC} and FF are expected to accompany a reduction in surface recombination velocity through a reduction in surface defects (*39*), and are also in qualitative agreement with the increase in film PL and PL lifetime upon treatment. Higher concentrations of DPPP (4 mg/mL) decreased short-circuit current density (J_{SC}) and FF, which may be resulted from the overreaction between DPPP and perovskites. Figure 4A shows *J-V* scans of the champion control and DPPP (2 mg/mL)-treated devices with 0.1 cm^2 aperture masks under forward and reverse scans. The PCE of the DPPP-treated device improved from 22.6% to 24.5%, with the V_{OC} increased from ~1.11 to ~1.16 V and FF increased from ~79% to ~82% (see detailed device parameters in table S1). External quantum efficiency (EQE) spectra (Fig. 4B) verified the J_{SC} values obtained from the *J-V* measurement. The enhanced EQE at short wavelengths also indicates improved carrier extraction at the front interface, which may be associated with the passivated interface achieved through the use of DPPP. We have also fabricated PSCs with a larger active area (1.05 cm^2) to validate the benefits of DPPP treatment. The target devices with DPPP treatment also showed overall improvement in device parameters (fig. S18), with the champion target device showing PCEs of 23.9% and 23.6% under reverse and forward scans (fig. S19 and table S2). The improvement on FF and V_{OC} confirmed the reduction on defect density at the NiO_x/perovskite front interface after DPPP treatment.

For durability tests, we replaced the Ag electrodes by Cr/Cu to avoid instability caused by Ag corrosion and diffusion but slightly lowered the device efficiency (by ~ 4 %) (fig. S20). We used 0.1 cm^2 aperture masks for solar cells when conducting all the stability tests. We first tested the effect of DPPP on device stability by maximum power point tracking (MPPT) under continuous 1 sun illumination in N_2 environment and at a temperature of ~40 °C. As shown in Fig. 4C, the DPPP-treated device exhibited an initial PCE of ~23%, increased to ~23.5% after ~450 hours and maintained unchanged after 3,500 hours. The increased PCE was contributed by the increased voltage at MPP (fig. S21), which is likely due to the light-induced annihilation of halide defects (*10, 40-43*). However, the PCE of the control device decreased to <80% of its initial PCE after 1,000 hours. The film area of the control PSC turned dark yellow, indicating the decomposition of perovskite to PbI_2 after 3,500 hours (fig. S22). In contrast, the film area of the DPPP-treated device remained dark, indicating more stabilized perovskite after DPPP treatment.

We then conducted accelerated durability tests at elevated temperatures. We kept the PSCs in a dark oven at 85°C and in the ambient, and measured the PCEs periodically for the thermal stress test (ISOS-D-2). We tested 18 PSCs and summarize their statistics in fig. S23. The average PCEs and their corresponding standard deviations (Fig. 4D) reveal that the DPPP-treated devices retain on average ~90% of their initial PCE after 1500 hours, while, in contrast, the average PCE of the control devices dropped to <90% after 168 hours.

We conducted a more rigorous accelerated durability test under the OC condition and continuous ~0.9 sun illumination. The devices were kept in an oven at a temperature of 85 °C and humidity of ~65% and measured every 208 s. The devices measured at 85 °C showed slightly lower PCEs possibly due to the negative temperature coefficient (fig. S24). The PCE was stable for the first ~300 hours and then slightly increased to ~108% of its initial value and showed no degradation after 1,500 hours (Fig. 4E). However, the control device degraded rapidly after 400 hours, dropping to ~80% of its initial PCE. Two more DPPP-treated PSCs were measured to validate the improved stability by DPPP treatment (fig. S25). The photos of devices after 1,500 hours of illumination were shown in fig. S26. The glass-side view of the control film turned gray, which was likely the result of delamination of the perovskite film at the NiO_x/perovskite front interface and the degradation of the perovskite layer. In contrast, the DPPP-treated device showed partial delamination on the edge but remained dark in most of the film area.

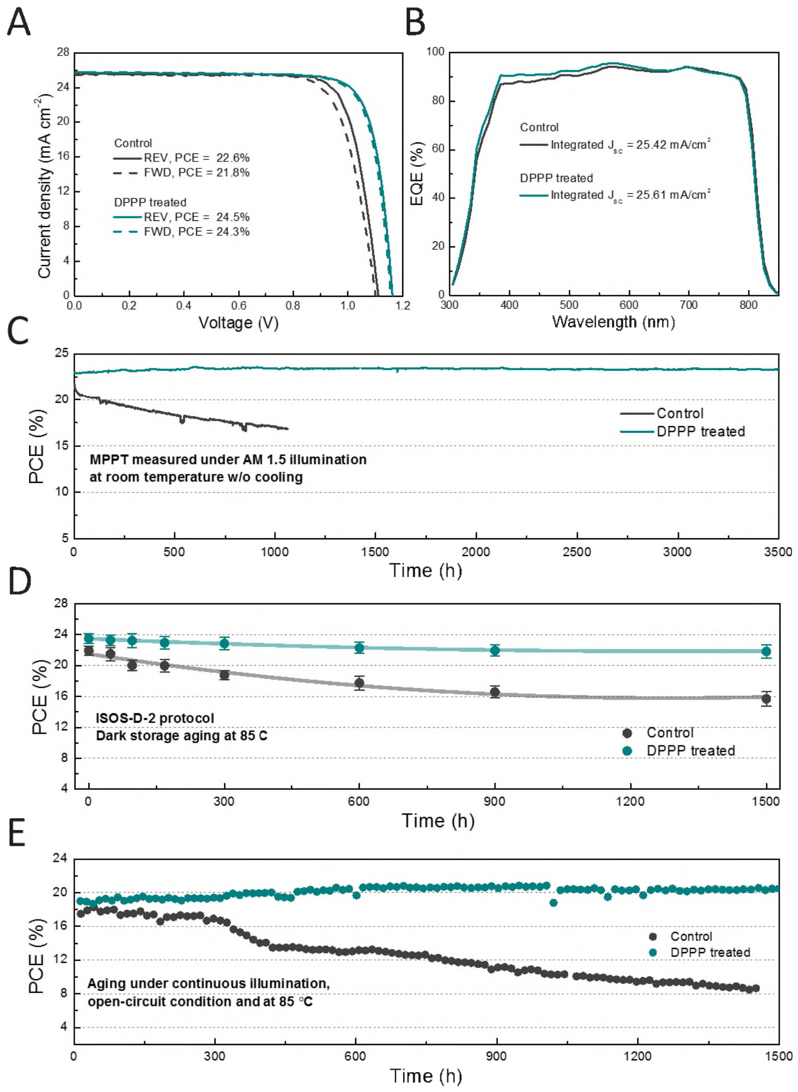

Fig. 4. Performance and stability of control and DPPP-treated devices. (A) *J-V* curves of champion control and DPPP treated devices. **(B)** EQE spectra of the corresponding control and DPPP-treated devices. **(C)** MPPT of control and DPPP-treated devices measured under continuous one sun illumination in N_2 environment and at a temperature of ~40 °C. **(D)** Thermal stress test of control and DPPP-treated devices aged at 85 °C following the ISOS-D-2 protocol. **(E)** Tracking of control and DPPP-treated devices measured at 85 °C and under continuous ~0.9 sun illumination and OC condition.

Discussion

Taking experimental findings together with DFT studies, we offer that DPPP molecules strengthen the NiO_x/perovskite interface and stabilize the perovskite phase. The robust binding between the NiO_x and perovskite enabled by DPPP modification appears to be an enabler of the stable operation of PSCs under outdoor conditions. The measured stability under accelerated testing conditions indicates a benefit from DPPP in improving device stability and provides ways to realizing commercialization of PSCs.

Reference and Notes

1. A. K. Jena, A. Kulkarni, T. Miyasaka, Halide perovskite photovoltaics: background, status, and future prospects. *Chem. Rev.* **119**, 3036-3103 (2019).
2. Z. Li *et al.*, Scalable fabrication of perovskite solar cells. *Nat. Rev. Mater.* **3**, 18017 (2018).
3. H. Min *et al.*, Perovskite solar cells with atomically coherent interlayers on SnO_2 electrodes. *Nature* **598**, 444-450 (2021).
4. Y. Zhao *et al.*, Inactive $(PbI_2)_2RbCl$ stabilizes perovskite films for efficient solar cells. *Science* **377**, 531-534 (2022).
5. Y. Rong *et al.*, Challenges for commercializing perovskite solar cells. *Science* **361**, eaat8235 (2018).
6. L. Meng, J. You, Y. Yang, Addressing the stability issue of perovskite solar cells for commercial applications. *Nat. Commun.* **9**, 5265 (2018).
7. P. Holzhey, M. Saliba, A full overview of international standards assessing the long-term stability of perovskite solar cells. *J. Mater. Chem. A* **6**, 21794-21808 (2018).
8. K. Domanski, E. A. Alharbi, A. Hagfeldt, M. Grätzel, W. Tress, Systematic investigation of the impact of operation conditions on the degradation behaviour of perovskite solar cells. *Nat. Energy* **3**, 61-67 (2018).
9. M. V. Khenkin *et al.*, Consensus statement for stability assessment and reporting for perovskite photovoltaics based on ISOS procedures. *Nat. Energy* **5**, 35-49 (2020).
10. R. Azmi *et al.*, Damp heat–stable perovskite solar cells with tailored-dimensionality 2D/3D heterojunctions. *Science* **376**, 73-77 (2022).
11. C. C. Boyd *et al.*, Understanding degradation mechanisms and improving stability of perovskite photovoltaics. *Chem. Rev.* **119**, 3418-3451 (2018).
12. M.-c. Kim *et al.*, Imaging real-time amorphization of hybrid perovskite solar cells under electrical biasing. *ACS Energy Lett.* **6**, 3530-3537 (2021).
13. E. Bi, Z. Song, C. Li, Z. Wu, Y. Yan, Mitigating ion migration in perovskite solar cells. *Trends in Chemistry* **3**, 575-588 (2021).
14. K. Domanski *et al.*, Migration of cations induces reversible performance losses over day/night cycling in perovskite solar cells. *Energy Environ. Sci.* **10**, 604-613 (2017).
15. T. Duong *et al.*, Light and electrically induced phase segregation and its impact on the stability of quadruple cation high bandgap perovskite solar cells. *ACS Appl. Mater.*

Interfaces **9**, 26859-26866 (2017).

16. B. Chen *et al.*, Synergistic effect of elevated device temperature and excess charge carriers on the rapid light-induced degradation of perovskite solar cells. *Adv. Mater.* **31**, 1902413 (2019).
17. Y. Yuan, J. Huang, Ion migration in organometal trihalide perovskite and itsimpact on photovoltaic efficiency and stability. *Acc. Chem. Res.* **49**, 286-293 (2016).
18. L. Shi *et al.*, Accelerated lifetime testing of organic–inorganic perovskite solar cells encapsulated by polyisobutylene. *ACS Appl. Mater. Interfaces* **9**, 25073-25081 (2017).
19. S. Yang *et al.*, Stabilizing halide perovskite surfaces for solar cell operation with wide-bandgap lead oxysalts. *Science* **365**, 473-478 (2019).
20. Y.-H. Lin *et al.*, A piperidinium salt stabilizes efficient metal-halide perovskite solar cells. *Science* **369**, 96-102 (2020).
21. S. Bai *et al.*, Planar perovskite solar cells with long-term stability using ionic liquid additives. *Nature* **571**, 245-250 (2019).
22. Z. Li *et al.*, Organometallic-functionalized interfaces for highly efficient inverted perovskite solar cells. *Science* **376**, 416-420 (2022).
23. T.-H. Han *et al.*, Perovskite-polymer composite cross-linker approach for highly-stable and efficient perovskite solar cells. *Nat. Commun.* **10**, 520 (2019).
24. M. Zhu *et al.*, Interaction engineering in organic–inorganic hybrid perovskite solar cells. *Mater. Horiz.* **7**, 2208-2236 (2020).
25. D. W. deQuilettes et al., Photoluminescence lifetimes exceeding 8 μs and quantum yields exceeding 30% in hybrid perovskite thin films by ligand passivation. *ACS Energy Lett.* **1**, 438-444 (2016).
26. C. Shi *et al.*, Molecular hinges stabilize formamidinium-based perovskite solar cells with compressive strain. *Adv. Funct. Mater.* 2201193 (2022).
27. Z. Yang *et al.*, Multifunctional phosphorus-containing Lewis Acid and Base passivation enabling efficient and moisture-stable perovskite solar cells. *Adv. Funct. Mater.* **30**, 1910710 (2020).
28. N. K. Noel *et al.*, Enhanced photoluminescence and solar cell performance via Lewis Base passivation of organic–inorganic lead halide perovskites. *ACS Nano* **8**, 9815-9821 (2014).
29. N. Ahn *et al.*, Highly reproducible perovskite solar cells with average efficiency of 18.3%

and best efficiency of 19.7% fabricated via Lewis base adduct of lead (II) iodide. *J. Am. Chem. Soc.* **137**, 8696-8699 (2015).

30. A. Seidu, M. Dvorak, J. Järvi, P. Rinke, J. Li, Surface reconstruction of tetragonal methylammonium lead triiodide. *APL Mater.* **9**, 111102 (2021).
31. S. Tan *et al.*, Surface reconstruction of halide perovskites during post-treatment. *J. Am. Chem. Soc.* **143**, 6781-6786 (2021).
32. D. W. de Quilettes et al., Impact of microstructure on local carrier lifetime in perovskite solar cells. *Science* **348**, 683-686 (2015).
33. Z. Song *et al.*, Probing the origins of photodegradation in organic–inorganic metal halide perovskites with time-resolved mass spectrometry. *Sustain. Energy Fuels* **2**, 2460-2467 (2018).
34. F. Fu *et al.*, I_2 vapor-induced degradation of formamidinium lead iodide based perovskite solar cells under heat–light soaking conditions. *Energy Environ. Sci.* **12**, 3074-3088 (2019).
35. J. Wang et al., Reducing surface recombination velocities at the electrical contacts will improve perovskite photovoltaics. *ACS Energy Lett.* **4**, 222-227 (2019).
36. J. A. Christians *et al.*, Tailored interfaces of unencapsulated perovskite solar cells for >1,000 hour operational stability. *Nat. Energy* **3**, 68-74 (2018).
37. W. Nie *et al.*, Light-activated photocurrent degradation and self-healing in perovskite solar cells. *Nat. Commun.* **7**, 11574 (2016).
38. G. Kresse, J. Furthmüller, Efficient iterative schemes for ab initio total-energy calculations using a plane-wave basis set. *Phys. Rev. B.* **54**, 11169-11186 (1996).
39. G. Kresse, J. Furthmüller, Efficiency of ab-initio total energy calculations for metals and semiconductors using a plane-wave basis set. *Comput. Mater. Sci.* **6**, 15-50 (1996).
40. P. E. Blöchl, Projector augmented-wave method. *Phys. Rev. B.* **50**, 17953-17979 (1994).
41. J. P. Perdew, K. Burke, M. Ernzerhof, Generalized gradient approximation made simple. *Phys. Rev. Lett.* **77**, 3865-3868 (1996).
42. S. Grimme, J. Antony, S. Ehrlich, H. Krieg, A consistent and accurate ab initio parametrization of density functional dispersion correction (DFT-D) for the 94 elements H-Pu. *J. Chem. Phys.* **132**, 154104 (2010).
43. A. R. M. Alghamdi, M. Yanagida, Y. Shirai, G. G. Andersson, K. Miyano, Surface passivation of sputtered NiO_x using a SAM interface layer to enhance the performance of

perovskite solar cells. *ACS Omega* **7**, 12147-12157 (2022).

44. G. Kresse, J. Furthmüller, Efficient iterative schemes for ab initio total-energy calculations using a plane-wave basis set. *Phys. Rev. B.* **54**, 11169-11186 (1996).
45. G. Kresse, J. Furthmüller, Efficiency of ab-initio total energy calculations for metals and semiconductors using a plane-wave basis set. *Comput. Mater. Sci.* **6**, 15-50 (1996).
46. P. E. Blöchl, Projector augmented-wave method. *Phys. Rev. B.* **50**, 17953-17979 (1994).
47. J. P. Perdew, K. Burke, M. Ernzerhof, Generalized gradient approximation made simple. *Phys. Rev. Lett.* **77**, 3865-3868 (1996).
48. S. Grimme, J. Antony, S. Ehrlich, H. Krieg, A consistent and accurate ab initio parametrization of density functional dispersion correction (DFT-D) for the 94 elements H-Pu. *J. Chem. Phys.* **132**, 154104 (2010).
49. A. R. M. Alghamdi, M. Yanagida, Y. Shirai, G. G. Andersson, K. Miyano, Surface passivation of sputtered NiO_x using a SAM interface layer to enhance the performance of perovskite solar cells. *ACS Omega* **7**, 12147-12157 (2022).

Acknowledgments

This material is based upon work supported by the U.S. Department of Energy’s Office of Energy Efficiency and Renewable Energy (EERE) under the Solar Energy Technologies Office Award Numbers DE-EE0008970 and DE-EE0008753, and by the U.S. Air Force Research Laboratory under agreement number FA9453-21-C-0056. F. J. and D. S. G.’s contributions, focusing on hyperspectral imaging for cell metrology, are based primarily on work supported by EERE under the Solar Energy Technologies Office (Award Number DE-EE0009528) as well as institutional support from the B. Seymour Rabinovitch Endowment and state of Washington. DFT calculations were supported by the Center for Hybrid Organic-Inorganic Semiconductors for Energy (CHOISE), an Energy Frontier Research Center funded by the Office of Basic Energy Sciences, Office of Science within the U.S. Department of Energy and the National Science Foundation under contract number DMR-1807818. The DFT calculations were performed using computational resources sponsored by the Department of Energy's Office of Energy Efficiency and Renewable Energy and located at the National Renewable Energy Laboratory and the DOS calculations used resources of the National Energy Research Scientific Computing Center (NERSC), a U.S. Department of Energy Office of Science User Facility located at Lawrence Berkeley National Laboratory, operated under Contract No. DE-AC02-05CH11231 using

NERSC award BES-ERCAP0017591. The U.S. Government is authorized to reproduce and distribute reprints for Governmental purposes notwithstanding any copyright notation thereon. The views expressed are those of the authors and do not reflect the official guidance or position of the United States Government, the Department of Defense or of the United States Air Force. The appearance of external hyperlinks does not constitute endorsement by the United States Department of Defense (DoD) of the linked websites, or the information, products, or services contained therein. The DoD does not exercise any editorial, security, or other control over the information you may find at these locations. Approved for public release; distribution is unlimited. Public Affairs release approval #AFRL-2022-3776. C.L. acknowledges Dr. Deying Luo for important discussions about the XPS analysis.

Author contributions:

C.L. and Y.Y. conceived the idea. Y.Y. supervised the projects and process. C.L., S.M.P. and E.B. fabricated perovskite films and devices for characterization and performance measurement. X.W. and Y.X. carried out DFT calculations. C.L., L.C., T.Z. and L.Z. carried out SEM, UV-vis and XRD measurements and data analysis. Z.S. carried out time-resolved mass spectroscopy measurement and data analysis. F.J. and D.S.G. carried out hyperspectral microscope measurement and associated data analysis. C.L. and J.C. prepared NiO_x substrates. Y.L. carried out stability tests and data analysis. Z.W., Y.L. and H.C. carried out XPS measurements and data analysis. H.L. and F.F. carried out the Tof-SIMS measurements and data analysis. C.R.G. carried out tensile force measurements and data analysis. A.A. and R.J.E carried out the PL and TRPL measurement and data analysis. C.L., X.W., S.Z., and Y.Y. wrote the first draft of the manuscript. E.H.S. and Y.Y. reviewed and edited the manuscript. All authors discussed the results and contributed to the revisions of the manuscript.

Competing interests: C.L. and Y.Y are inventors on a patent application related to this work filed by the University of Toledo. The other authors declare no competing interests.

Data and materials availability: All data are available in the main text or the supplementary materials.

Supplementary Materials

Materials and Methods

Figs. S1 to S26

Tables S1 to S2